

Digital instability of a confined elastic meniscus

John S. Biggins^{a,b}, Baudouin Saintyves^c, Zhiyan Wei^a, Elisabeth Bouchaud^{c,d}, and L. Mahadevan^{a,e,f,g,1}

^fWyss Institute for Biologically Inspired Engineering, ^gKavli Institute for Bionano Science and Technology, ^aSchool of Engineering and Applied Sciences, and ^bDepartment of Physics, Harvard University, Cambridge, MA 02138; ^cCavendish Laboratory, University of Cambridge, Cambridge CB3 0HE, United Kingdom; ^dCommissariat à l'Energie Atomique, Institut Rayonnement Matière de Saclay, Service de Physique de l'Etat Condensé, F-91191 Gif-sur-Yvette Cedex, France; and ^eEcole Supérieure de Physique et de Chimie Industrielles ParisTech, Unité Mixte de Recherche Gulliver, 75231 Paris Cedex 5, France

Edited* by Grigory Isaakovich Barenblatt, University of California, Berkeley, CA, and approved June 4, 2013 (received for review February 6, 2013)

Thin soft elastic layers serving as joints between relatively rigid bodies may function as sealants, thermal, electrical, or mechanical insulators, bearings, or adhesives. When such a joint is stressed, even though perfect adhesion is maintained, the exposed free meniscus in the thin elastic layer becomes unstable, leading to the formation of spatially periodic digits of air that invade the elastic layer, reminiscent of viscous fingering in a thin fluid layer. However, the elastic instability is reversible and rate-independent, disappearing when the joint is unstressed. We use theory, experiments, and numerical simulations to show that the transition to the digital state is sudden (first-order), the wavelength and amplitude of the fingers are proportional to the thickness of the elastic layer, and the required separation to trigger the instability is inversely proportional to the in-plane dimension of the layer. Our study reveals the energetic origin of this instability and has implications for the strength of polymeric adhesives; it also suggests a method for patterning thin films reversibly with any arrangement of localized fingers in a digital elastic memory, which we confirm experimentally.

hysteresis | confinement | elastomer | gel

In adhesive joints, the strains and stresses due to joint loading are magnified by the effects of geometric confinement and scale separation (1), making them susceptible to stress-driven instabilities that often lead to failure. Joints usually fail in one of two broad ways: via adhesive failure along the solid–solid interface (2–5) or via bulk cohesive failure of the glue joint via cavitation (6–8). Though these modes of failure have been well documented and studied (see ref. 1 for a review), there is a third mode of failure, where an elastic instability at the meniscus may lead to fracture in its vicinity and can arise either when a joint is loaded under tension (9) or by a fluid that is injected into a cavity in the confined elastic layer (10). This mode of failure has been largely overlooked experimentally and is not understood theoretically. Interestingly, the last experiment is an elastic analog of a well-studied classical hydrodynamic free-surface instability associated with the relative motion between liquids of different viscosities in a narrow gap (11, 12), and provides a point for comparison. As we will see, the elastic instability is fundamentally different given its reversible nature and lack of dependence on interfacial forces. We use a combination of theory, experiment, and computation to unravel the mechanism behind the elastic meniscus instability, the threshold strain for its onset, the critical wavelength of the resulting fingers, and the nonlinear development of its amplitude.

Geometrically, our setup, sketched in Fig. 1A, consists of a thin, highly elastic layer occupying the region $-a/2 < z < a/2$, $-\infty < x < \infty$, $0 < y < l$ with $a/l \ll 1$ that is adhered to rigid plates at $z = \pm a/2$. Experimentally, we used a layer of polyacrylamide gel with a shear modulus of 550 Pa, thickness $a \in [0.28, 10.64]$ mm, and width $l \in [50, 60]$ mm bound between 10-mm-thick glass plates that were ~ 200 mm long. The plates are then pulled apart, increasing their separation to $a + \Delta z$, while maintaining adhesion. Experimentally, the separation was increased at a constant speed of ~ 200 mm/s. As the rigid plates are separated, the free boundaries of the elastomer (at $y = 0$ and $y = l$) retreat to form an elastic

meniscus that is curved in the direction perpendicular to the plates but remains parallel to its original position, thus penetrating into the elastic film without causing any loss of adhesion to the glass plates. At a critical separation of the plates, this curved meniscus loses stability via a sharp transition to an undulatory configuration in which fingers of air protrude into the elastomer, shown schematically in Fig. 1A. To ensure that elastic equilibrium was achieved at each stage, and to rule out any rate dependence, we also performed experiments at much lower velocities and saw quantitatively similar results.

Fig. 1B shows the undulatory pattern observed. We note that this instability is qualitatively different from the crack-like adhesive undulatory instabilities seen at the glass–gel contact line when adhesion starts to fail (2). In our experiments, adhesion is maintained everywhere due to the natural propensity of polyacrylamide to stick strongly to glass. Thus, fingers appear along the retreating elastic meniscus. Fig. 1B also shows a loading/unloading hysteresis loop for the transition, showing that the instability sets in suddenly past a given threshold in displacement via a subcritical instability, leading to large amplitude “digits” or fingers whose amplitude grows further upon further loading (Movie S1). On unloading, the fingers snap back at a lower value of the displacement, suggestive of the hysteretic nature of this first-order transition (Movie S2). We find that the undulatory transition is fully reversible and has no dependence on the shear modulus of the elastomer, strongly suggesting that the phenomenon is purely elastic. The similarity in the small smooth part of the loading and unloading curves, which corresponds to a plate separation of $\sim 1.5\%$ at most, is likely due to inhomogeneities in the meniscus when it was first formed via our molding protocol. To test this, we waited for up to 30 min after the destabilization of the front, and did not see any additional fingers form. On retracing the loading/unloading cycle, we saw that the system traced the same curves as the first time, consistent with this explanation. Finally, we performed identical experiments in oil rather than in air to determine the effect of surface tension on the instability (Movie S3), and find that the system responds just as when it is in air, eliminating a role for the effects of surface tension in the phenomenon. It is useful to contrast these observations with the case of viscous fingering (11), where fingering is dynamic and out of equilibrium, and surface tension effects cannot be neglected.

Because the deformations involved are large, we resorted to numerical simulations of the process in terms of a finite element method, using an incompressible neo-Hookean constitutive model for the elastic layer. To capture the subcritical nature of the instability, we needed to carry out a dynamical simulation

Author contributions: J.S.B., Z.W., and L.M. designed and carried out theoretical and computational research; B.S. and E.B. designed experiments and analyzed experimental data; B.S. performed experiments; and J.S.B. and L.M. wrote the paper.

The authors declare no conflict of interest.

*This Direct Submission article had a prearranged editor.

¹To whom correspondence should be addressed. E-mail: lm@seas.harvard.edu.

This article contains supporting information online at www.pnas.org/lookup/suppl/doi:10.1073/pnas.1302269110/-DCSupplemental.

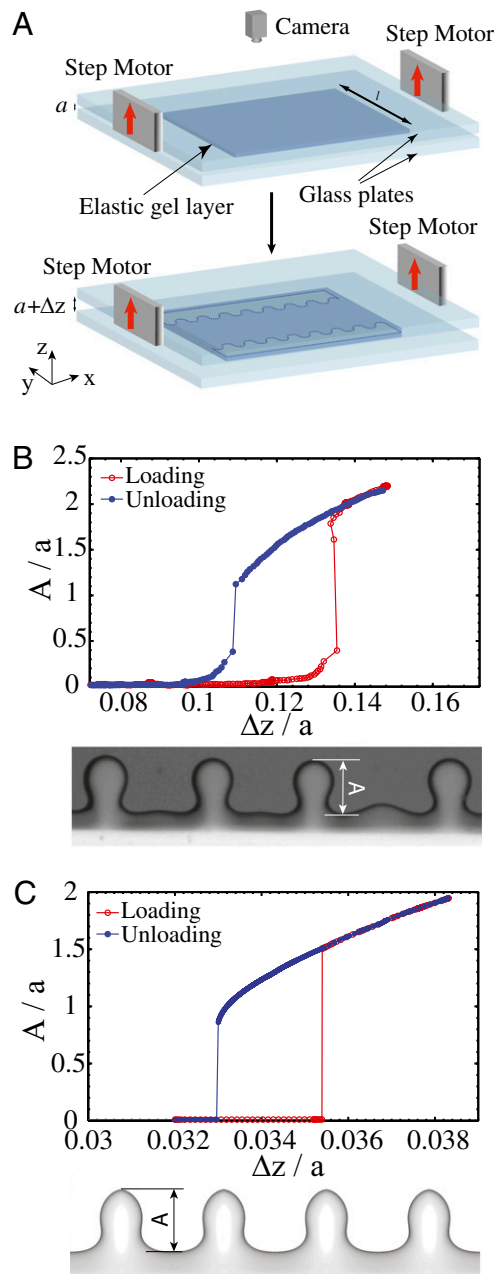


Fig. 1. (A) Schematic of an elastic layer between two rigid plates. Pulling the plates apart causes the two free menisci to lose stability by forming a series of undulating digital fingers. (B) The experimentally measured amplitude of the fingers as a function of plate separation Δz , along with a top view of the undulating meniscus showing the fingers of air (Lower) invading the elastic layer (Upper). The layer thickness is $a = 3.05$ mm and the width is $l = 56$ mm. Observe the hysteresis in the transition associated with the difference between the loading and unloading curves. (C) Numerical results for an identical quasi-static loading and unloading protocol (SI Appendix, Numerical Simulations) calculated using a finite element method for an elastic layer of thickness $a = 1$ mm and width $l = 40$ mm show the same qualitative features—a hysteretic transition (Upper) associated with the formation of undulating fingers (Lower).

with damping, modeled via a Rayleighian dissipation function. The boundary conditions were imposed using the symmetry of the problem, and a small amount of initial noise in the position of the meniscus was used to seed the instability. All numerical simulations were carried out using a commercial finite element package ABAQUS (SI Appendix, Numerical Simulations), allowing us to reproduce this instability. We note that once the fingers

develop and have a finite amplitude, they may not be described by a single-valued function, but this is not an issue in our simulations, which use a natural coordinate system for the meniscus. In Fig. 1C, we show that both the form of the fingers and the hysteresis loop associated with a loading/unloading loop arise in a purely elastic simulation.

To understand our experiments and numerical simulations, we start by estimating the energies and length-scales in the problem. Displacement of a point in the central plane of the elastomer by an amount $u \sim a$ in the y direction of the x – y plane leads to a shear strain in the elastomer $\gamma \sim u/a$. Because the subcritical fingering transition is purely elastic, it is likely to occur at large strains with a threshold $\gamma \sim 1$ when geometrically nonlinear effects are important. Incompressibility of the elastomer implies that $\Delta z \sim ua$, so that the instability threshold $\Delta z_i \sim O(a^2/l)$, which vanishes for infinitesimally thin films when $l/a \rightarrow \infty$. We note that this threshold arises from purely geometric considerations and expect that it does not depend on any material properties, because the only energy scale in the system, the shear modulus, can be scaled away. Furthermore, if fingers form with wavelength λ and amplitude A , this introduces additional strain associated with the in-plane distortion of magnitude A/λ . At the onset of the instability, the elastic screening length $O(a)$ must scale with the thickness of the layer, so that we expect the wavelength of the instability to also be independent of any material parameters, with $\lambda \sim O(a)$. However, how is it that the formation of fingers, which are areas that have receded deeply into the bulk and therefore undergone huge shear strains, can reduce the total shear energy in the elastomer?

To clarify how fingering can alleviate shear, we first build a very simple model completely neglecting in-plane strain. Again, focusing our attention on the central plane of the elastomer, we assume that it is made of thin strips of width dx , which we treat as elastically independent. If one of these strips is stretched in-plane by a factor λ_y in the y direction and a factor λ_x in the x direction, as shown in Fig. 2A and B, the small thickness of the strip guarantees that the displacements in the x direction are small compared with a , and therefore do not give rise to large shear strains. However, a point with coordinate y is moved by an amount $(y-l/2)(1-\lambda_y)$ and so suffers a strain $\gamma \sim (y-l/2)(1-\lambda_y)/a$, and the elastic shear energy of the strip is therefore $E_s \propto \int_0^l \gamma^2 dy \propto (1-\lambda_y)^2$. A stretch in the z direction by a factor of $(1+\Delta z/a)$, together with volume conservation requires $(1+\Delta z/a)\lambda_x\lambda_y = 1$, which allows us to rewrite the shear energy of our strip as $E_s \propto (1+\Delta z/a - 1/(\lambda_x))^2$. Plotting this as a function of λ_x in Fig. 2C, we see that the energy has a minimum at $\lambda_x = 1/(1+\Delta z/a) < 1$ for $\Delta z > 0$. However, because our system is infinite in the x direction, we know that the average x -stretch $\langle \lambda_x \rangle = 1$; otherwise, the strips will build up infinite displacements in the x direction. Inspecting Fig. 2C, we see a large nonconvex region extending from the minimum till $\lambda_x \rightarrow \infty$, i.e., the total energy of the system is minimized when $\Delta z > 0$ with most strips being stretched by the optimal value of $\lambda_x = 1/(1+\Delta z/a) < 1$ and a very small number having large λ_x ; these digits dig deep into the bulk of the elastomer, leading to the fingering instability. We note that if the energy was convex, the minimum energy compatible with the average stretch $\langle \lambda_x \rangle = 1$ would be achieved by each strip individually taking $\lambda_x = 1$. This simple explanation thus accounts for how the lack of convexity drives the energetics of finger formation and predicts a first-order transition to a large-amplitude state, consistent with the experimentally observed hysteresis shown in Fig. 2B.

Though our zero-dimensional model provides a mechanism for the instability, it is unable to provide information about the wavelength and threshold for the instability; for this, we now turn to an asymptotic simplification of the 3D problem by taking advantage of the small thickness and symmetry of the elastic layer. We expand the displacement vector $U(x, y, z)$ to leading

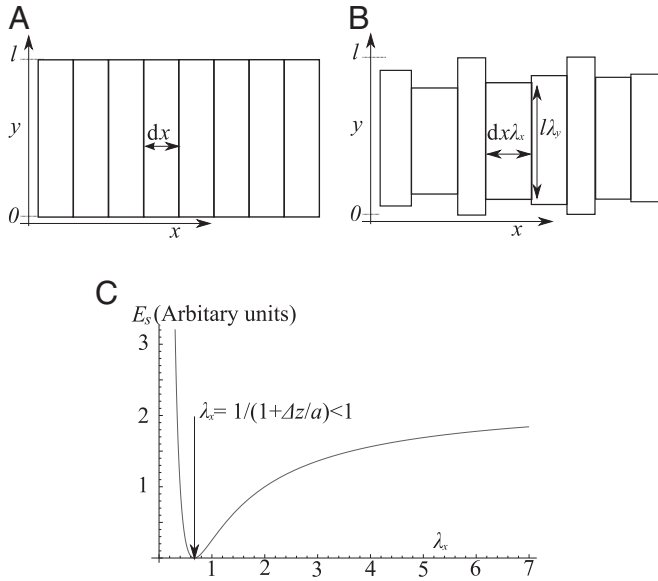


Fig. 2. (A) The simplest model that characterizes the phenomenon focuses on the central ($z=0$) plane of the elastomer and considers it to be composed of many independent thin strips of width dx . (B) A schematic of the deformation of the strips when stretched perpendicular to the plane of the paper leads them to undergo independent planar deformations. (C) The constraint of incompressibility causes the energy of a strip E_s to not be a convex function of λ_x so the minimal average energy with $\langle \lambda_x \rangle = 1$ is achieved by most strips taking the optimal value of contraction and a small number taking divergent values and hence receding deeply into the bulk and forming fingers. This minimal model highlights the mechanism of instability but provides no information about the wavelength and threshold for the instability (see text).

order in z and impose the condition that $\mathbf{U} = \pm \Delta z \hat{\mathbf{z}}/2$ at $z = \pm a/2$, leading to the form

$$\mathbf{U} = (1 - 2z/a)(1 + 2z/a)\mathbf{u}(x, y) + (z\Delta z/a)\hat{\mathbf{z}}, \quad [1]$$

where $\mathbf{u}(x, y)$ is the 2D displacement of a point on the central ($z=0$) plane. With ∇ as the in-plane gradient operator and I as the 2D identity matrix, we can then write the 3D deformation gradient, $F_{ij} = \delta_{ij} + \partial_j U_i$, as

$$F = I + (1 - 4z^2/a^2)\nabla\mathbf{u} - 8z\mathbf{u}\hat{\mathbf{z}}/a + (1 + \Delta z/a)\hat{\mathbf{z}}\hat{\mathbf{z}}, \quad [2]$$

and see the decomposition that results as a consequence of scale separation.

To characterize the energetic cost of this deformation, we model the elastomer as an incompressible neo-Hookean solid with volumetric elastic energy density $\frac{1}{2}\mu\text{Tr}(F.F^T)$, which we can explicitly integrate in the thickness direction. Here we assume that surface tension effects are unimportant, as our experiments show. Thus, when the energy of the system is rescaled by this single constant, what remains is a purely geometric problem. The constraint of volume preservation in the elastomer when integrated through the depth requires us to introduce a 2D pressure field $P(x, y)$ that constrains the depth-averaged volume change at each point in the elastomer, and leads us to an effective 2D energy density L :

$$L(\mathbf{u}, P) = \mu \int_{-a/2}^{a/2} \frac{1}{2} \text{Tr}(F.F^T) - \frac{P(\text{Det}(F) - 1)}{1 + \Delta z/a} dz$$

$$\propto \frac{1}{2} \text{Tr}(G.G^T) + \frac{16}{5} |\mathbf{u}/a|^2 - P \left(\text{Det}(G) - 1 + \frac{6}{5} \Delta z/a \right). \quad [3]$$

In carrying out the integral (*SI Appendix, Theoretical Model*), we have introduced an effective 2D deformation gradient $G = I + \frac{4}{5}\nabla\mathbf{u}$ and, because we expect $\Delta z/l \sim a^2/l \ll a$, retained only the leading-order term in $\Delta z/a$. We note that $\frac{\partial L}{\partial \nabla\mathbf{u}} = \frac{4}{5}(G - P\text{Det}(G)G^{-T})$, so extremizing this energy leads to the following Euler-Lagrange equations for the planar displacement field \mathbf{u} and the pressure P ,

$$\frac{4}{5}\nabla^2\mathbf{u} - \text{Det}(G)G^{-T} \cdot \nabla P = 8\mathbf{u}/a^2$$

$$\text{Det}(G) = 1 - \frac{6}{5}\Delta z/a. \quad [4]$$

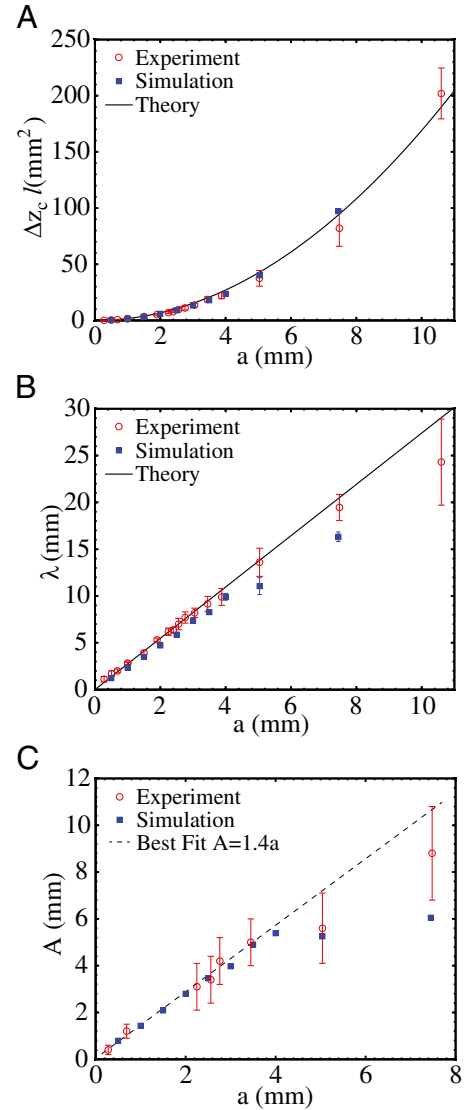


Fig. 3. Comparison of experimental and theoretical/numerical predictions. (A) Threshold separation $\Delta z_c \times \text{width } l$ as a function of thickness a shows that the experimental and numerical results follow the theoretical prediction (Eqs. 13 and 14). (B) Finger wavelength λ at instability as a function of thickness a shows that the experimental and numerical results follow the theoretical prediction (Eqs. 13 and 14). (C) Finger amplitude A just after threshold as a function of thickness a shows that the experimental and numerical results agree, but only over a range of thickness values. For large a , the separation of scales between the thickness a and width of the film l is less, and the number of wavelengths in the sample is smaller, leading to end effects that make agreement between theory and experiment only qualitative.

It is interesting to note that the form of the depth-integrated Eq. 4 is similar to the Darcy–Brinkman equation for flow through a dilute porous media (13), with the displacement reinterpreted as a velocity. Here, the most interesting aspect of the equation is the appearance of the bare displacement of the central plane \mathbf{u} . On the free surfaces $y=0, l$, we must satisfy the natural boundary condition

$$(G - P \text{Det}(G)G^{-T}) \cdot \hat{\mathbf{y}} = 0. \quad [5]$$

Taking each field to be the sum of a large translationally invariant base state corresponding to the deformations before the instability and an infinitesimal oscillation in the x direction, we may write

$$\mathbf{u} = Y_1(y)\hat{\mathbf{y}} + \epsilon \cos(kx)Y_2(y)\hat{\mathbf{y}} + \epsilon \sin(kx)X_2(y)\hat{\mathbf{x}} \quad [6]$$

$$P = 1 + P_1(y) + \epsilon \cos(kx)P_2(y). \quad [7]$$

Substituting this into [4]–[5] and solving for the translationally invariant fields, we get

$$Y_1(y) = \frac{3}{4} \Delta z(l - 2y)/a \quad [8]$$

$$P_1(y) = 6y\Delta z(y - l)/a^3 - \frac{6}{5} \Delta z/a. \quad [9]$$

At order ϵ , the Euler–Lagrange equations (Eq. 4) can be solved algebraically for X_2 and P_2 to yield a linear fourth-order eigenvalue equation for Y_2 , whose solution provides us the wavelength and threshold for instability (*SI Appendix, Theoretical Model*). A substantial simplification arises by considering the limit $l \gg a$ and, consequently, $\Delta z \ll a$, which allows us to drop all terms proportional to Δz except those also containing powers of l , reducing the final equation to

$$(a^2k^2 + 10)a^2k^2Y_2(y) + a^4Y_2^{(4)}(y) = 2(a^2k^2 + 5)a^2Y_2''(y), \quad [10]$$

which has the allowable decaying solutions

$$Y_2 = c_1 \exp\left(-\sqrt{10/a^2 + k^2}y\right) + c_2 \exp(-ky). \quad [11]$$

Substituting this into Eq. 5 gives $c_1 = -c_2k^2/(5/a^2 + k^2)$ and a condition which yields the threshold separation Δz_t for instability at wavenumber k

$$\Delta z_t = \frac{a^2 \left(a^2k^2 - \sqrt{a^2k^2 + 10}ak + 10 \right) a^2k^2 + 25}{15ak}. \quad [12]$$

Minimizing this expression with respect to k yields the threshold of the first unstable mode (Δz_t) and the wavelength (λ), which are given by

$$\Delta z_t \approx 1.69a^2/l \quad [13]$$

$$\lambda \approx 2.74a.$$

[14]

We see that the wavelength of the instability scales with the thickness of the elastic layer and the threshold displacement is inversely proportional to the slab width, and are independent of any material parameters, as we argued earlier based on scaling arguments.

In Fig. 3, we show a comparison of these predictions with experiments and numerical simulations (*SI Appendix, Numerical Simulations*); the results compare very well. Although our linearized analysis cannot extend beyond the point of instability, our finite element simulations have no such limit. Experimental and numerical results show that the amplitude of the fingers $A \approx 1.4a$, and confirm the subcritical nature of the instability with a region of bistability wherein the homogeneous and undulatory phases of the interface coexist. In this regard, our elastic instability is fundamentally different from the hydrodynamic Saffman–Taylor instability that is supercritical.

Our study has uncovered the form and nature of the confined elastic meniscus fingering instability in a minimal rectilinear setting using a combination of theory, experiment, and numerical simulation. We show the origin of the transition is essentially geometric and hence likely to be ubiquitous, just as its fluid counterpart is, and predict and verify the wavelength and threshold of the instability. At a practical level, our results have implications for the strength of elastic adhesive layers; because the peak strain jumps very significantly during the fingering transition, fingering is very likely to lead to fracture and adhesive failure. From our 2D model, the stored energy per unit area scales as $\mu a(\Delta z/l/a^2)^2$, so that the normal stress that must be applied to the plates $\sigma_t \sim \mu l/a$, and predicts that the fracture stress of polymeric adhesives is inversely proportional to the thickness of the layer, and that the total strength of the adhesive bond increases faster than the adhesion area.

We have also shown that the transition is sudden with a region of bistability between the fingered and flat states. The hysteretic nature of the transition permits control over the placement of fingers or digits; if the system is in the bistable regime one may “write” out arbitrary “bits” onto the interface by applying a large perturbation at the desired location (*Movie S4*). These bits are completely reversible localized elastic structures, so that this fingering transition might be used to build a digital mechanical memory. Because our system produces fingers with wavelength proportional to the smallest length-scale in the problem—namely, the thickness of the layer—without any pre patterning on this length-scale, this mechanism may also have uses in microfabrication. Although the digitization instability is fully reversible, it may be easily made permanent by further cross-linking; additionally, the use of a nematic elastomer may allow the transition to be driven by heat or light rather than separation.

ACKNOWLEDGMENTS. This work was supported by the Royal Society (J.S.B.), the French ANR F2F project (E.B.), the MacArthur Foundation (L.M.), and Grant DMR0820484 from Harvard-MRSEC NSF (Materials Research Science and Engineering Centers, National Science Foundation).

- Shull KR (2002) Contact mechanics and the adhesion of soft solids. *Mater Sci Eng Rep* 36(1):1–45.
- Ghatak A, Chaudhury MK, Shenoy V, Sharma A (2000) Meniscus instability in a thin elastic film. *Phys Rev Lett* 85(20):4329–4332.
- Monch W, Herminghaus S (2001) Elastic instability of rubber films between solid bodies. *Europhys Lett* 53(4):525–531.
- Adda-Bedia M, Mahadevan L (2006) Crack-front instability in a confined elastic film. *Proc R Soc A* 462(2075):3233–3251.
- Vilmin T, Ziebert F, Raphaël E (2010) Simple view on fingering instability of debonding soft elastic adhesives. *Langmuir* 26(5):3257–3260.
- Gent A, Lindley PB (1959) Internal rupture of bonded rubber cylinders in tension. *Proc R Soc A* 249(1257):195–205.
- Crosby AJ, Shull KR, Lakrout H, Creton C (2000) Deformation and failure modes of adhesively bonded elastic layers. *J Appl Phys* 88(5):2956–2966.

- Shull KR, Creton C (2004) Deformation behavior of thin compliant layers under tensile loading conditions. *J Polym Sci B Polym Phys* 42(22):4023–4043.
- Shull KR, Flanigan CM, Crosby AJ (2000) Fingering instabilities of confined elastic layers in tension. *Phys Rev Lett* 84(14):3057–3060.
- Saintyves B, Dauchot O, Bouchaud E (2012) Bulk elastic fingering instability in Hele-Shaw cells. *Phys Rev Lett*, in press.
- Saffman PG, Taylor GI (1958) The penetration of a fluid into a porous medium or Hele-Shaw cell containing a more viscous liquid. *Proc R Soc Lond A* 245(1242):312–329.
- Homsy GM (1987) Viscous fingering in porous media. *Annu Rev Fluid Mech* 19:271–311.
- Brinkman HC (1949) A calculation of the viscous force exerted by a flowing fluid on a dense swarm of particles. *Appl Sci Res* 1(1):27–34.

Supplementary Information for
“Digital instability of a confined elastic
meniscus”
by Biggins et al.

May 22, 2013

1 Movies

The enclosed movies show the formation of the instability and our ability to pattern it in the bistable regime.

Movie1:

Typical experiment for a gap $a = 3.05mm$, showing a sinusoidal destabilization just before the sudden nucleation of a finger. Dimension of slab $29 \times 20mm$. The movie is slowed down by a factor of 20.

Movie2:

Movie showing the reversibility of the instability and its hysteretic character. The transient domain is relatively small compared to the size of a finger. Gap $a = 3.04mm$. Dimension of slab $13 \times 19mm$. Real speed.

Movie3:

Movie showing that identical fingering occurs even when the air-elastomer interface is replaced by an air-oil interface. The change in interfacial tension does not change either the onset of the instability or its wavelength, suggesting that the effects of interfacial tension are unimportant at leading order in determining this phenomenon.

Movie4:

Movie showing the possibility to nucleate a finger wherever along the front in the hysteretic region, when the two plates have been separated by a distance $\Delta z = 0.36mm$. The needle used to poke the gel is made of hydrophobic plastic. Gap $a = 3.04mm$. Dimension of slab $27 \times 19mm$. Real speed.

2 Theoretical model

Our two-dimensional elastic model of the instability successfully predicts the wavelength and threshold without any fitting parameters. Here, we provide further details of the theory associated with the calculations of the thickness integral of the energy and the stability analysis of the model.

We recall that we are modeling an elastic solid initially occupying the region of space $-\infty < x < \infty$, $0 < y < l$, $-a/2 < z < a/2$ where $a \ll l$ and which is perfectly adhered to rigid glass plates at $z = \pm a/2$. The glass plates are then moved further apart by an amount Δz so that they are at $z = \pm(a + \Delta z)/2$ and we seek to understand the response of the elastomer to this loading.

2.1 Quadratic form of the displacement and deformation gradient (eqns. (1) and (2))

The displacement of a point in the elastomer initially at (x, y, z) is $\mathbf{U}(x, y, z)$. Taking advantage of the thinness of the elastomer, we Taylor expand this displacement to quadratic order in z giving

$$\mathbf{U}(x, y, z) = \mathbf{A}(x, y) + z\mathbf{B}(x, y) + z^2\mathbf{C}(x, y) + \dots \quad (\text{S.1})$$

Imposing symmetry about $z = 0$ we see that \mathbf{B} lies in the $\hat{\mathbf{z}}$ direction while \mathbf{A} and \mathbf{C} lie in the $x - y$ plane. Requiring that $\mathbf{U}(x, y, \pm a/2) = \pm \Delta z \hat{\mathbf{z}}/2$ so that the displacement on the boundaries matches that of the plates, we see that $\mathbf{B} = \Delta z \hat{\mathbf{z}}/a$ and that $\mathbf{A} = -(a^2/4)\mathbf{C}$. Since \mathbf{A} is the displacement of a point in the $z = 0$ plane and lies entirely in the $z = 0$ plane, we write $\mathbf{A} = \mathbf{u}$ so the entire displacement becomes

$$\mathbf{U}(x, y, z) = (1 - 4z^2/a^2)\mathbf{u}(x, y) + (z\Delta z/a)\hat{\mathbf{z}}, \quad (\text{S.2})$$

which corresponds to eqn. (1) in the article.

The deformation gradient F is defined as $F_{ij} = \delta_{ij} + \partial_j U_i$. Using ∇ as the in-plane gradient operator (i.e. $\nabla = \hat{\mathbf{x}} \frac{\partial}{\partial x} + \hat{\mathbf{y}} \frac{\partial}{\partial y}$) and I as the in-plane identity ($I = \hat{\mathbf{x}}\hat{\mathbf{x}} + \hat{\mathbf{y}}\hat{\mathbf{y}}$) we can evaluate F as

$$F = I + (1 - 4z^2/a^2)\nabla\mathbf{u} - 8z\mathbf{u}\hat{\mathbf{z}}/a^2 + (1 + \Delta z/a)\hat{\mathbf{z}}\hat{\mathbf{z}}, \quad (\text{S.3})$$

which is eqn. (2) in the article.

Working in an $x - y - z$ basis and breaking \mathbf{u} into components as $\mathbf{u} = u_x \hat{\mathbf{x}} + u_y \hat{\mathbf{y}}$ we can write F explicitly as

$$F = \begin{pmatrix} 1 + (1 - \frac{4z^2}{a^2}) \frac{\partial u_x}{\partial x} & (1 - \frac{4z^2}{a^2}) \frac{\partial u_x}{\partial y} & -\frac{8zu_x}{a^2} \\ (1 - \frac{4z^2}{a^2}) \frac{\partial u_y}{\partial x} & 1 + (1 - \frac{4z^2}{a^2}) \frac{\partial u_y}{\partial y} & -\frac{8zu_y}{a^2} \\ 0 & 0 & 1 + \Delta z/a \end{pmatrix}. \quad (\text{S.4})$$

2.2 2-D Energy Function (eqn. (3))

We write our two dimensional elastic energy as

$$L(\mathbf{u}, P) = \mu \int_{-a/2}^{a/2} \frac{1}{2} \text{Tr} (F.F^T) - \frac{P(x, y)(\text{Det}(F) - 1)}{1 + \Delta z/a} dz, \quad (\text{S.5})$$

where the first term is a standard neo-hookean energy density for a deformed elastomer, and the second term models the elastomers incompressibility by imposing thickness averaged incompressibility at every point in the $x - y$ plane via a pressure-like Lagrange multiplier field $P(x, y)$. The coefficient of this term is simply for algebraic convenience. Evaluating the first term in this integral is a simple matter of expanding $\text{Tr} (F.F^T)$ and integrating each term separately:

$$\begin{aligned} \text{Tr} (F.F^T) &= 2 + (1 - 4z^2/a^2)^2 \text{Tr} (\nabla \mathbf{u} (\nabla \mathbf{u})^T) + \\ &64z^2 \mathbf{u} \cdot \mathbf{u} / a^4 + (1 + \Delta z/a)^2 + 2(1 - 4z^2/a^2) \nabla \cdot \mathbf{u} \end{aligned} \quad (\text{S.6})$$

$$\begin{aligned} \int_{-a/2}^{a/2} \text{Tr} (F.F^T) dz &= a(2 + (1 + \Delta z/a)^2) + \frac{4a}{3} \nabla \cdot \mathbf{u} \\ &+ \frac{8a}{15} \text{Tr} (\nabla \mathbf{u} (\nabla \mathbf{u})^T) + \frac{16}{3a} \mathbf{u} \cdot \mathbf{u} \end{aligned} \quad (\text{S.7})$$

$$= \frac{5a}{6} \text{Tr} (G.G^T) + \frac{16}{3a} \mathbf{u} \cdot \mathbf{u} + \text{const} \quad (\text{S.8})$$

In the last line we have introduced an effective two dimensional deformation gradient $G = I + \frac{4}{5} \nabla \mathbf{u}$.

The second term in the energy can be treated in a similar way. We first note that $\text{Det}(F) = (1 + \Delta z/a) \text{Det}(I + (1 - 4z^2/a^2) \nabla \mathbf{u})$. Secondly, we use the (two-dimensional) relation that $\text{Det}(I + cB) = 1 + c \text{Tr} (B) + c^2 \text{Det}(B)$

to expand $\text{Det}(F)$ then integrate each term separately giving:

$$\int_{-a/2}^{a/2} \text{Det}(F) dz = a \left(1 + \frac{\Delta z}{a} \right) \times \left(1 + \frac{2}{3} \text{Tr}(\nabla \mathbf{u}) + \frac{8}{15} \text{Det}(\nabla \mathbf{u}) \right). \quad (\text{S.9})$$

Applying the same identity, this can be rewritten as $a(1 + \Delta z/a)(5\text{Det}(G) + 1)/6$. Assembling these two results, we can write the entire integrated energy as

$$L = \frac{5\mu a}{6} \left(\frac{1}{2} \text{Tr}(G.G^T) + \frac{16}{5} \frac{\mathbf{u} \cdot \mathbf{u}}{a^2} - P \left(\text{Det}(G) - 1 + \frac{6\Delta z}{5(a + \Delta z)} \right) + \text{const} \right). \quad (\text{S.10})$$

Finally, we neglect the constant, drop the pre-factor and, since $\Delta z_t \sim a^2/l \ll l$, replace $\Delta z/(a + \Delta z)$ by $\Delta z/a$, to write

$$L \propto \frac{1}{2} \text{Tr}(G.G^T) + \frac{16}{5} |\mathbf{u}/a|^2 - P \left(\text{Det}(G) - 1 + \frac{6}{5} \Delta z/a \right),$$

which corresponds to eqn. (3) in the main article.

2.3 Bulk equations and boundary conditions (eqns. (4)-(5))

We now seek to minimize the total energy of the elastomer, so we find the Euler-Lagrange equations for \mathbf{u} and P :

$$\partial_j \frac{\partial L}{\partial \partial_j u_i} = \frac{\partial L}{\partial u_i} \quad (\text{S.11})$$

$$\frac{\partial L}{\partial P} = 0 \quad (\text{S.12})$$

The second of these straightforwardly evaluates to give

$$\text{Det}(G) = 1 - \frac{6}{5} \Delta z/a. \quad (\text{S.13})$$

The right-hand side of the first equation is also straightforward: $\partial L/\partial u_i = (5\mu a/6)(32/5)u_i/a^2$. The left-hand side can be evaluated using the result that $\partial \text{Det}(A)/\partial A_{ij} = \text{Det}(A) A_{ij}^{-T}$, so we have

$$\frac{\partial L}{\partial \partial_j u_i} = \frac{5\mu a}{6} \left(\frac{4}{5} G_{ij} - \frac{4}{5} P \text{Det}(G) G_{ij}^{-T} \right). \quad (\text{S.14})$$

To construct the whole equation we need one final result, $\partial_j \text{Det}(G) G_{ij}^{-T} = 0$, which is easily seen by explicitly writing out G . We can then write the entire equation as

$$\frac{4}{5}a^2 \nabla^2 \mathbf{u} - \text{Det}(G) G^{-T} \cdot a^2 \nabla P = 8\mathbf{u}. \quad (\text{S.15})$$

Equations S.15 and S.13 correspond to eqn. (4) in the main article.

Since our problem does not impose any additional constraints at $y = 0, l$ we take the natural boundary conditions, corresponding to an unconstrained minimization of the energy, given by $\frac{\partial L}{\partial \partial_j u_i} \hat{n}_j = 0$ where $\hat{\mathbf{n}}$ is the unit normal vector at the boundary. In our case $\hat{\mathbf{n}} = \hat{\mathbf{y}}$ on both boundaries. We have already evaluated this derivative, so we can immediately write the boundary condition as

$$(G - P \text{Det}(G) G^{-T}) \cdot \hat{\mathbf{y}} = 0. \quad (\text{S.16})$$

corresponding to eqn. (5) in the main article.

2.4 Solving the model (eqns. (6) to (14))

To solve our model, we introduce a trial form for the solutions consisting of a large translationally invariant part and an infinitesimal oscillatory part:

$$\mathbf{u} = Y_1(y) \hat{\mathbf{y}} + \epsilon \cos(kx) Y_2(y) \hat{\mathbf{y}} + \epsilon \sin(kx) X_2(y) \hat{\mathbf{x}} \quad (\text{S.17})$$

$$P = 1 + P_1(y) + \epsilon \cos(kx) P_2(y). \quad (\text{S.18})$$

The translationally invariant part corresponds to the deformations before the fingering instability, which we call the base-state. Working in the $x - y$ coordinate system we have

$$G_1 = \begin{pmatrix} 1 & 0 \\ 0 & 1 + \frac{4}{5} Y_1'(y) \end{pmatrix}, \quad (\text{S.19})$$

and

$$\text{Det}(G_1) G_1^{-T} = \begin{pmatrix} 1 + \frac{4}{5} Y_1'(y) & 0 \\ 0 & 1 \end{pmatrix}. \quad (\text{S.20})$$

Substituting G_1 into eqn. S.13 we get

$$\frac{4}{5} Y_1'(y) = -\frac{6}{5} \Delta z / a, \quad (\text{S.21})$$

which we can solve for Y_1 to get

$$Y_1(y) = \frac{3\Delta z(l - 2y)}{4a}, \quad (\text{S.22})$$

in which we have fixed the constant on integration by requiring that $Y_1(l/2) = 0$ to preserve the symmetry about $y = l/2$. This corresponds to eqn. (8) in the main article. Since $\nabla P = P'_1(y)\hat{y}$, we can write eqn. S.15 as

$$\frac{4}{5}a^2Y_1''(y) - a^2P'_1(y) = 8Y_1(y). \quad (\text{S.23})$$

This can be integrated to find

$$P_1(y) = 6y\Delta z(y - l)/a^3 - \frac{6}{5}\Delta z/a. \quad (\text{S.24})$$

This corresponds to eqn. (9) in the main article. The constant of integration has been found by applying the boundary condition (eqn. S.16) which reads:

$$(\frac{4}{5}Y'_1(y) - P_1(y))|_{y=0,l} = 0. \quad (\text{S.25})$$

We consider adding an infinitesimal oscillatory perturbation to the base-state to examine its stability. We now have

$$G = G_1 + \frac{4\epsilon}{5} \begin{pmatrix} k \cos(kx)X_2(y) & \sin(kx)X'_2(y) \\ -k \sin(kx)Y_2(y) & \cos(kx)Y'_2(y) \end{pmatrix}, \quad (\text{S.26})$$

$$\begin{aligned} \text{Det}(G) G^{-T} &= \text{Det}(G_1) G_1^{-T} \\ &+ \frac{4\epsilon}{5} \begin{pmatrix} \cos(kx)Y'_2(y) & k \sin(kx)Y_2(y) \\ -\sin(kx)X'_2(y) & k \cos(kx)X_2(y) \end{pmatrix}. \end{aligned} \quad (\text{S.27})$$

Substituting G into eqn. S.13 and expanding to first (linear) order in ϵ gives

$$\epsilon \cos(kx)((1 + \frac{4}{5}Y'_1(y))kX_2(y) + Y'_2(y)) = 0 \quad (\text{S.28})$$

Recalling the form of $Y_1(y)$ we see that

$$Y'_1(y) = -\frac{3\Delta z}{2a}. \quad (\text{S.29})$$

We expect the threshold value of Δz to scale as $\Delta z_t \sim a^2/l$ so, in the limit of $a \ll l$, we expect $\Delta z_t \ll a$ and hence $Y'_1(y) \ll 1$. This means we can neglect $Y'_1(y)$ in the above equation, so the solution for $X_2(y)$ is simply

$$X_2(y) = -Y'_2(y)/k. \quad (\text{S.30})$$

We can also write ∇P as

$$\nabla P = \begin{pmatrix} -\epsilon k \sin(kx)P_2(y) \\ P'_1(y) + \epsilon P'_2(y) \cos(kx) \end{pmatrix}, \quad (\text{S.31})$$

so the x component of eqn. S.15 is, to linear order in ϵ ,

$$\begin{aligned} \frac{4}{5}a^2(X_2''(y) - k^2X_2(y)) \\ + a^2((1 + \frac{4}{5}Y_1'(y))kP_2(y) - \frac{4}{5}kY_2(y)P_1'(y)) = 8X_2(y) \end{aligned} \quad (\text{S.32})$$

We can again neglect $Y_1'(y) \ll 1$ term so, substituting in our solution for $X_2(y)$, we can solve algebraically for P_2 to get

$$P_2(y) = \frac{4}{5} \left(Y_2(y)P_1'(y) - \left(1 + \frac{10}{a^2k^2} \right) Y_2'(y) + \frac{Y_2'''(y)}{k^2} \right). \quad (\text{S.33})$$

Finally, we can evaluate the y component of eqn. S.15 to linear order in ϵ to get

$$\begin{aligned} \frac{4}{5}a^2(Y_2''(y) - k^2Y_2(y)) - a^2(P_2'(y) + \frac{4}{5}kX_2(y)P_1'(y)) \\ = 8Y_2(y). \end{aligned} \quad (\text{S.34})$$

Substituting in our results for $X_2(y)$ and $P_2(y)$ gives

$$\begin{aligned} k^2Y_2(y) (10 + a^2k^2 + a^2P_1''(y)) + a^2Y_2^{(4)}(y) \\ = 2(5 + a^2k^2)Y_2''(y). \end{aligned} \quad (\text{S.35})$$

Recalling the form of P_1 , we see that

$$a^2P_1''(y) = 12\Delta z/a \quad (\text{S.36})$$

so, as with $Y_1'(y)$, we see that $a^2P_1''(y) \ll 1$ when $a \ll l$ so we can ignore $P_1''(y)$ in the above equation giving

$$\begin{aligned} a^2k^2Y_2(y) (10 + a^2k^2) + a^4Y_2^{(4)}(y) \\ = 2(5 + a^2k^2)a^2Y_2''(y), \end{aligned} \quad (\text{S.37})$$

which corresponds to eqn. (10) in the main article. We focus on the boundary at $y = 0$ and so look for solutions that decay as $y \rightarrow \infty$. We write Y_2 as a linear sum of the two such solutions

$$Y_2 = c_1 \exp\left(-\sqrt{10/a^2 + k^2}y\right) + c_2 \exp(-ky), \quad (\text{S.38})$$

which is equation (11) in the main article.

We impose the boundary condition at $y = 0$. Since these solutions decay as $y \rightarrow \infty$ we can neglect the boundary condition at $y = l$. The linear correction to the boundary condition at $y = 0$ (eqn. S.16) is

$$\frac{4}{5} \begin{pmatrix} X_2'(0) \\ Y_2'(0) \end{pmatrix} = P_2(0) \begin{pmatrix} 0 \\ 1 \end{pmatrix} + (1 + P_1(0)) \begin{pmatrix} \frac{4}{5}kY_2(0) \\ \frac{4}{5}kX_2(0) \end{pmatrix}. \quad (\text{S.39})$$

However, $P_1(0) = -\frac{6}{5}\Delta z/a \rightarrow 0$ when $a \ll l$ so the x component, after substituting for X_2 , is

$$-Y_2''(0) = k^2 Y_2(0). \quad (\text{S.40})$$

Substituting in our result for Y_2 we solve for c_2 to get

$$c_1 = -c_2 \frac{a^2 k^2}{5 + a^2 k^2}. \quad (\text{S.41})$$

The y component requires us to evaluate $P_2(0)$. To do this we first note that

$$-\left(1 + \frac{10}{a^2 k^2}\right) Y_2'(0) + \frac{Y_2'''(0)}{k^2} = \frac{10c_2}{a^2 k}, \quad (\text{S.42})$$

and secondly that $P_1'(0) = -6l\Delta z/a^3$, which does not vanish for $a \ll l$ because it contains a power of l . Assembling the entire boundary condition then gives

$$Y_2'(0) = -\frac{6l\Delta z}{a^3} Y_2(0) + \frac{10c_2}{a^2 k} - Y_2'(0), \quad (\text{S.43})$$

which, upon substituting for Y_2 and c_1 and solving algebraically for Δz_t gives

$$\Delta z_t = \frac{a^2}{l} \frac{25 + a^2 k^2 \left(10 + ak \left(ak - \sqrt{10 + a^2 k^2}\right)\right)}{15ak} \quad (\text{S.44})$$

which corresponds to eqn. (12) in the main article. This result tells us the threshold Δz at which a mode with wave-number k becomes unstable. We find the first unstable mode by minimizing this result over k , to predict that the first unstable mode has

$$\lambda \approx 2.74...a \quad (\text{S.45})$$

$$\Delta z_t \approx 1.69...a^2/l. \quad (\text{S.46})$$

which correspond to equations (13)-(14) in the main article.

3 Numerical Simulations

All simulations were performed using the commercial finite element software ABAQUS 6.11. A sketch of the simulation domain is shown in Fig. S.1. Although the transition under examination is purely elastic, its subcritical nature means that it cannot be simulated using equilibrium methods, so instead we use Newtonian dynamics with both numerical and viscous damping. We ran two types of simulations: lower resolution simulations

with many wavelengths to capture the behavior at onset and high resolution simulations focusing on a single digit to capture the profile of the fingers.

1. Material properties

The gel is modeled as an incompressible neo Hookean material with shear modulus of $500Pa$ and a density $10^3Kg/m^3$. We used a large Rayleigh damping model to ensure that the system is overdamped. For a given mode i the fraction of critical damping, ξ_i , can be expressed in terms of the damping factors α_R and β_R as:

$$\xi_i = \frac{\alpha_R}{2\omega_i} + \frac{\beta_R\omega_i}{2}, \quad (S.47)$$

where ω_i is the natural frequency at this mode, α_R is for mass proportional damping and β_R is for stiffness proportional damping. To define Rayleigh damping, we need to specify α_R and β_R . We load the boundary near the critical displacement and perform a linear perturbation procedure to extract ω_i , $i = 1$ to 5 , and correspondingly specify α_R to make ξ_i around 5 . This is only a crude estimation of the damping coefficient as the stiffness matrix is a function of strain. When the fingers are fully grown, we expect the natural frequency is different from that of the onset state. After a try and error, we set $\alpha_R = 8000$ to 10000 to damp out the lowest frequency oscillation. For the highest frequency, we rely on numerical damping (which will be documented later) and set $\beta_R = 0$.

2. Boundary conditions

Symmetric boundary conditions are applied on the two lateral planes (highlighted in yellow), the middle plane (light grey), and the back plane (blue). Therefore only a quarter of the physical thin slab is simulated to save computational power. The front surface (green) is stress free and Gaussian white noise is applied on its initial y coordinate in order to trigger the instability at the critical loading displacement. The mean magnitude of the noise is 2% of the smallest mesh size inside the system. The top surface is pulled apart at such a small constant velocity that it always takes 5 to 10 minutes before the top surface is loaded up to the critical displacement. Once oscillations of the front surface are detected, the pulling is stopped and the top surface is held still while the system evolves freely.

3. Meshes and elements

First, to get the displacement and wavelength of the onset of the instability, we run the simulation in a long cell (which contains 8 to 9 wavelengths) containing 401 nodes for the length, 76 nodes for the half-width and 26 nodes for the half-gap. This is more than adequate to detect the point of onset and the wavelength of the unstable mode, but, as the fingers grow, the strain at the tip of the fingers becomes very large (greater than 7) so we need a finer mesh. In order to capture the profile of the fully grown finger, we set the length of gel slab as half the previously calculated wavelength, and keep the boundary conditions the same. We use $201 \times 76 \times 26$ nodes to a quarter of a single finger, which is sufficient to resolve its full profile, even with the very large strains at its tip. Mesh density is geometrically biased towards the free front and middle plane, where the nonlinearity is the most pronounced after instability happens. C3D8H (8-node linear brick, hybrid with constant pressure) elements are adopted. The pressure penalty serves as an additional degree of freedom to ensure the constraint of incompressibility.

4. Time integrator

As the material is incompressible, it is impossible to simulate the dynamic response with an explicit method as the stable time increment would be inversely proportional to the bulk modulus. Therefore we use an implicit method. Both the Hilber-Hughes-Taylor (HHT) integrator and backward Euler integrator gave the same onset of instability and fastest growing mode. In our system, we did not resolve the high-frequency vibrations and used a large numerical dissipation to obtain convergence during the loading history. In the HHT scheme, we choose $\alpha = -1/3$, $\beta = 1/4(1 - \alpha)^2$ and $\gamma = 1/2 - \alpha$ to achieve the maximum numerical damping [1] with an adaptive time step which is reduced in the neighborhood of instability.

5. Dimensions of the samples

We choose layer dimensions to ensure that the ratio of the width to the gap thickness is large (over 10) so that the layer can reasonably be thought of as thin. Our choice of length containing 8-9 wavelengths was determined to keep a low overhead on the computational costs. We note that this causes some end-effects in our simulation, which explains why the calculated wavelength is slightly below our experimentally observed wavelength. Tab. 1 shows the sample dimensions used, while

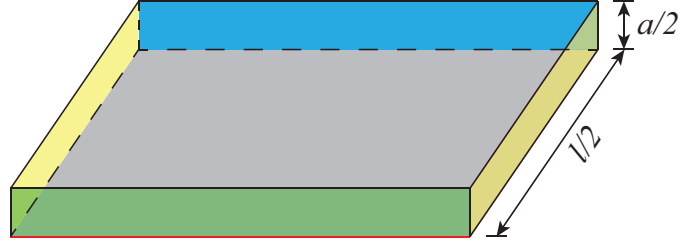


Figure S.1: Sketch of the simulation domain. Only a quarter of the thin slab is simulated. To detect whether the front surface (green) is oscillatory, we extract the displacement at the intersection line (red) where the middle plan (light grey) and front surface meet.

Table 1: Sample Dimensions (mm)

length	10	20	30	40	50	60	70	80	100.2	149
width	40	40	40	40	60	60	80	80	58.5	55.8
gap thickness	0.5	1.0	1.5	2.0	2.5	3.0	3.5	4.0	5.04	7.45

Fig. S.2 shows the 3D geometry of the fully grown finger right after the instability. Only one finger with periodic boundary conditions was actually simulated.

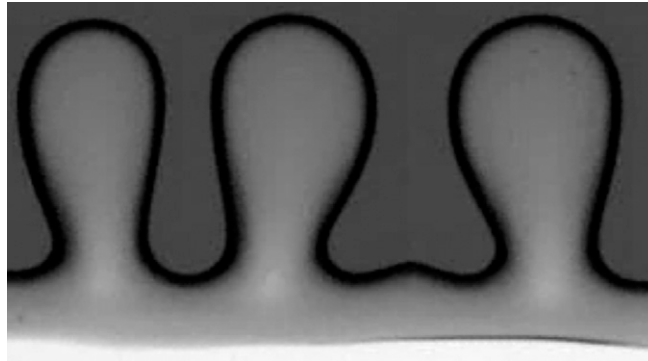
References

- [1] Hilber, H. M., T. J. R. Hughes, and R. L. Taylor, Improved Numerical Dissipation for Time Integration Algorithms in Structural Dynamics, Earthquake Engineering and Structural Dynamics, vol. 5, pp. 283C292, 1977.

Figure S.2: $3D$ geometry of a single finger right after the instability. Only one finger was simulated with periodic boundary conditions. ADOBE READER allows for the manipulation of this interactive figure.

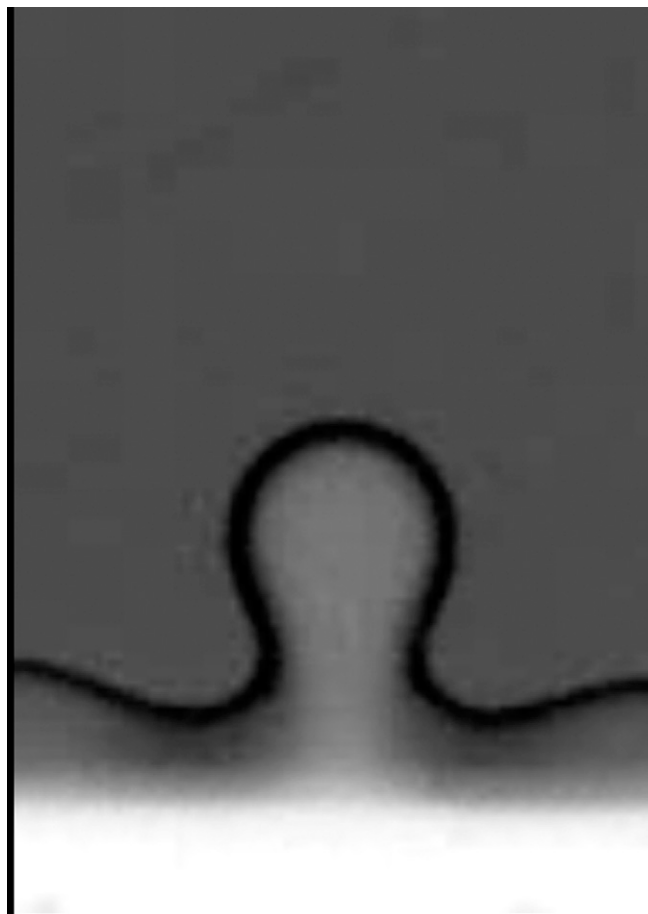
Supporting Information

Biggins et al. 10.1073/pnas.1302269110



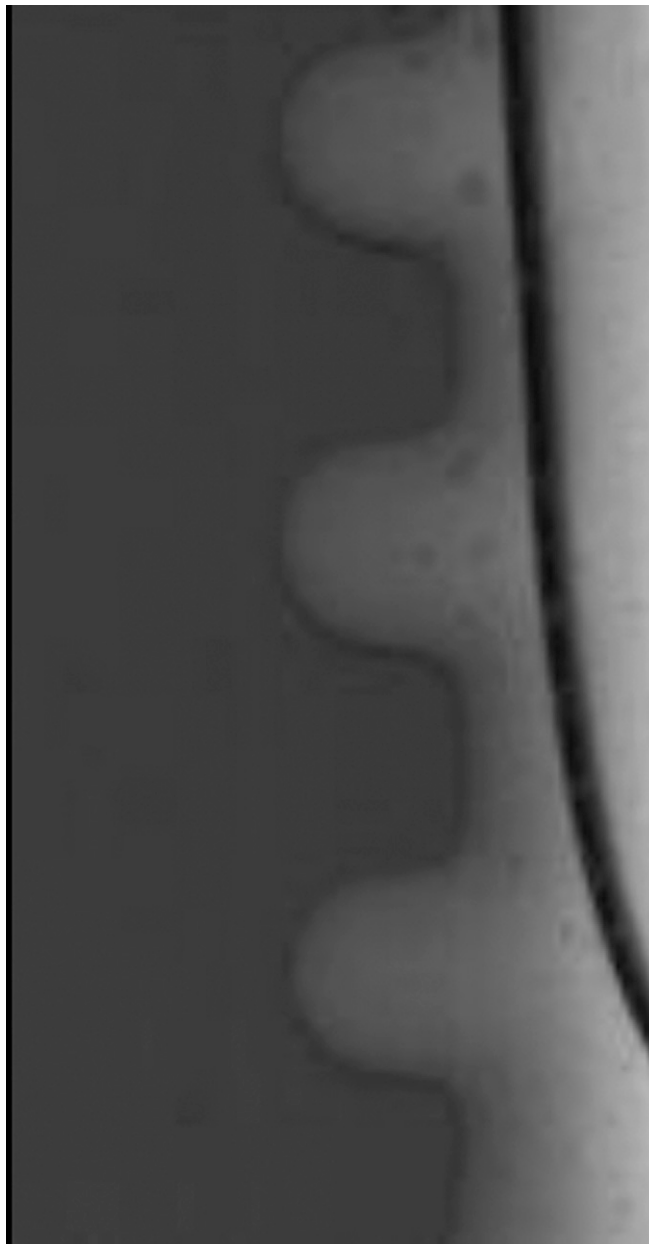
Movie S1. Typical experiment for a gap $a = 3.05$ mm, showing a sinusoidal destabilization just before the sudden nucleation of a finger. Dimension of slab: 29×20 mm. The movie is slowed down by a factor of 20.

[Movie S1](#)



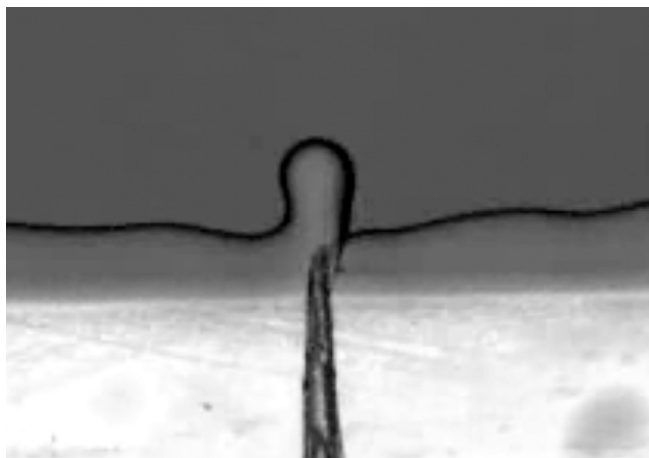
Movie S2. Movie showing the reversibility of the instability and its hysteretic character. The transient domain is relatively small compared to the size of a finger. Gap $a = 3.04$ mm. Dimension of slab: 13×19 mm. Real speed.

[Movie S2](#)



Movie S3. Movie showing that identical fingering occurs even when the air–elastomer interface is replaced by an air–oil interface. The change in interfacial tension does not change either the onset of the instability or its wavelength, suggesting that the effects of interfacial tension are unimportant at leading order in determining this phenomenon.

[Movie S3](#)



Movie S4. Movie showing the possibility to nucleate a finger wherever along the front in the hysteretic region, when the two plates have been separated by a distance $\Delta z = 0.36$ mm. The needle used to poke the gel is made of hydrophobic plastic. Gap $a = 3.04$ mm. Dimension of slab: 27×19 mm. Real speed.

[Movie S4](#)

Other Supporting Information Files

[SI Appendix \(PDF\)](#)